Heterogeneous Catalysis

International Edition: DOI: 10.1002/anie.201906256
German Edition: DOI: 10.1002/ange.201906256

Supported Intermetallic PdZn Nanoparticles as Bifunctional Catalysts for the Direct Synthesis of Dimethyl Ether from CO-Rich Synthesis Gas

*Manuel Gentzen, Dmitry E. Doronkin, Thomas L. Sheppard, Anna Zimina, Haisheng Li, Jelena Jelic, Felix Studt, Jan-Dierk Grunwaldt, Jörg Sauer, and Silke Behrens**

Abstract: *The single-step syngas-to-dimethyl ether (STD) process entails economic and technical advantages over the current industrial two-step process. Pd/ZnO-based catalysts have recently emerged as interesting alternatives to currently used $Cu/ZnO/Al_2O_3$ catalysts, but the nature of the active site(s), the reaction mechanism, and the role of Pd and ZnO in the solid catalyst are not well established. Now, Zn-stabilized Pd colloids with a size of 2 nm served as the key building blocks for the methanol active component in bifunctional $Pd/ZnO\text{-}\gamma\text{-}Al_2O_3$ catalysts. The catalysts were characterized by combining high-pressure operando X-ray absorption spectroscopy and DFT calculations. The enhanced stability, longevity, and high dimethyl ether selectivity observed makes $Pd/ZnO\text{-}\gamma\text{-}Al_2O_3$ an effective alternative system for the STD process compared to $Cu/ZnO/\gamma\text{-}Al_2O_3$.*

Dimethyl ether (DME) is industrially produced by dehydration of methanol derived from synthesis gas (CO/H_2), with a global production of 5 Mtons/year.[1] This two-step process typically employs $Cu/ZnO/Al_2O_3$ catalysts for methanol synthesis and solid acids (for example, γ-Al_2O_3 or zeolites) for methanol dehydration. The development of an alternative single-step STD process is highly desirable as it entails economic and technical advantages, for example, cost saving by process simplification and higher syngas conversions.[1] This necessitates the design of suitable bifunctional catalysts with high methanol synthesis and dehydration activity. Recent efforts have involved preparing physical mixtures of the two components[2] as well as bifunctional catalysts,[3] which couple the two sequential reactions on active sites in close proximity to each other. Conventional Cu/ZnO-based methanol catalysts have been one focus of study; however, these systems can be prone to deactivation, which drives the search for new catalysts.[4] Recently, Pd-based intermetallic compounds have emerged as interesting alternatives providing improved methanol selectivity and thermal stability. Pd/ZnO systems in particular have been successfully employed in methanol steam reforming (MSR)[5] and the water-gas-shift (WGS) reaction,[6] and have recently proven to be a suitable methanol synthesis component for the STD process in combination with a solid acid.[3b,7] The activity of these catalysts was ascribed to the formation of intermetallic PdZn during the reductive catalyst pretreatment.[3b,6,8]

While Pd/ZnO-based catalysts have been investigated experimentally and theoretically, for example, for MSR and WGS, the exact nature of the active site(s) and the reaction mechanism for bifunctional Pd/ZnO based STD catalysts is not well defined, and depends strongly on the synthesis route employed.[3b,7,9] Herein we focus on the colloidal synthesis of highly uniform Pd/Zn-based nanoparticles (NPs). This method allows for evenly distributed metal content, sizes, and shapes, which are ideal for mechanistic investigation using complementary spectroscopy, and computational modeling.[10] We show how Pd/Zn catalyzes the hydrogenation of CO to DME by employing high-pressure operando X-ray absorption spectroscopy (XAS), in conjunction with density functional theory (DFT) calculations.

Uniform Pd/Zn-based NPs were synthesized by reacting $Pd(acac)_2$ and Et_2Zn, yielding particles with the Pd core in close contact to the Zn-containing organic shell without the need for additional ligands or surfactants (Supporting Information). Since Pd^0 promotes the formation of methane over methanol, it is critical to avoid the formation of Pd^0 via reactive Pd^0-Zn^{2+} interfaces by ensuring the sufficient supply of Zn atoms during catalyst preparation and activation. This synthesis concept is versatile and provides various NP building blocks for the methanol-active component.[10a–c] TEM images revealed highly uniform Pd/Zn NPs of 2.0 ± 0.4 nm diameter (Figure 1a). The molar Pd:Zn ratio of the NP powder was 1:2.9, in agreement with the $Pd(acac)_2$:Et_2Zn

[*] Dr. M. Gentzen, Dr. D. E. Doronkin, Dr. T. L. Sheppard, Dr. A. Zimina, Dr. H. Li, Dr. J. Jelic, Prof. F. Studt, Prof. J.-D. Grunwaldt, Prof. J. Sauer, Dr. S. Behrens
Institute of Catalysis Research and Technology
Karlsruhe Institute of Technology (KIT)
Herrmann-von-Helmholtz-Platz 1
76344 Eggenstein-Leopoldshafen (Germany)
E-mail: silke.behrens@kit.edu
Dr. D. E. Doronkin, Dr. T. L. Sheppard, Dr. A. Zimina, Prof. F. Studt, Prof. J.-D. Grunwaldt
Institute for Chemical Technology and Polymer Chemistry
Karlsruhe Institute of Technology (KIT)
Engesserstr. 20, 76131 Karlsruhe (Germany)
Dr. H. Li
School of Physics and Engineering
Henan University of Science and Technology
471023 Luoyang, Henan Province (P. R. China)
Supporting information and the ORCID identification number(s) for the author(s) of this article can be found under: https://doi.org/10.1002/anie.201906256.

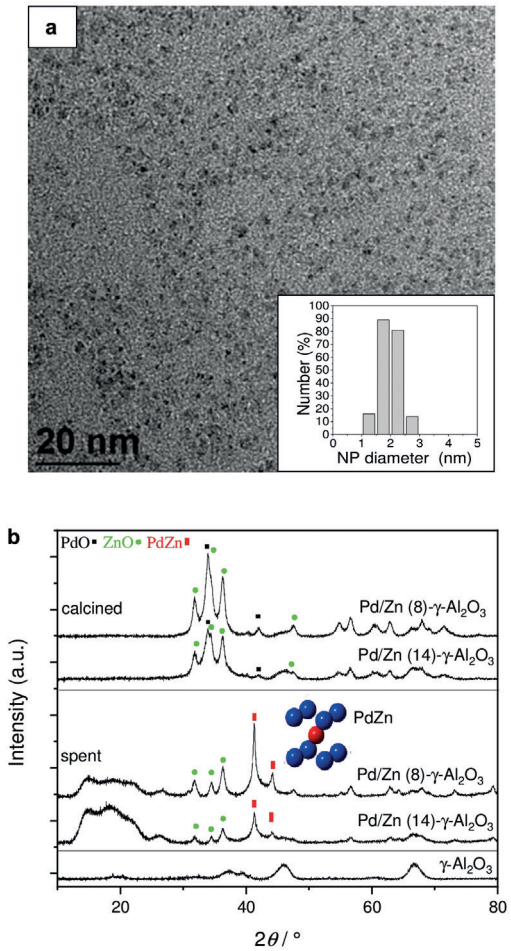

Figure 1. a) TEM image of the Pd/Zn NPs (inset: particle size distribution). b) XRD patterns of the calcined and spent Pd/Zn-based STD catalysts (inset: PdZn structure (*P4/mmm*; Pd blue, Zn red).

ratio used during synthesis. After deposition on γ-Al_2O_3 and calcination, two bifunctional STD catalysts with Pd loadings of 8.4 wt% (Pd/Zn (8)-γ-Al_2O_3) and 14.3 wt% (Pd/Zn (14)-γ-Al_2O_3) were obtained (see the Supporting Information, Table S1, for elemental composition, specific surface area, number of acid sites).

X-ray diffraction (XRD) of the calcined STD catalysts showed reflections of PdO, Pd, ZnO, and γ-Al_2O_3 (Figure 1b) and no reflections from mixed oxides or alloyed species. Following catalytic tests, the spent catalysts revealed reflections at 41.2° and 44.1° (2θ) characteristic of the $L1_0$ PdZn phase, respectively, and no Pd^0 reflections (Figure 1b). Topotactic alloy formation involves considerable reduction of ZnO in close contact to a noble metal capable of dissociative H_2 adsorption (that is, Pd). Since NP synthesis afforded a molar Pd/Zn ratio of 1:3, sufficient Zn was available for complete formation of an intermetallic PdZn phase. Residual Zn^{2+} species remained as ZnO in the spent STD catalyst. According to the Scherrer equation, particle sizes were 8–11 nm for PdO and 16 nm for PdZn in the calcined and spent catalysts, respectively. TEM and SEM images of the calcined and spent catalysts revealed Pd/Zn-based NPs well distributed over the Al_2O_3 dehydration catalyst (Supporting Information, Figure S1), facilitating close proximity between the consecutive catalytic functions of methanol synthesis and dehydration.

The catalytic properties of the bifunctional PdZn catalysts in the STD reaction were determined in a fixed-bed reactor (50 bar, 250–300 °C, 70 vol% inert gas (Ar/N_2); Supporting Information, Table S2) using syngas with a H_2/CO composition of 1:1, simulating that derived from renewable biomass feedstock. For Pd/Zn (8)-γ-Al_2O_3, CO conversion increased with temperature until a maximum at 290 °C (X_{CO} 37%; Figure 2b). At higher temperatures, thermodynamic equilibrium constraints become more important, resulting in decreased CO conversion of 34% at 300 °C.

PdZn alloys showed good selectivity to DME while maintaining high activity (S_{DME} 65% at 250–270 °C, S_{DME} 62% at 300 °C). CH_4 formation was negligible between 250 °C and 280 °C ($S_{CH4} < 1\%$) and increased only slightly to 2.4% at 300 °C. In contrast, Pd_2Ga NPs showed a lower DME and a higher CH_4 selectivity.[10c] The ratio of methanol to dehydration catalyst is also known to influence catalytic

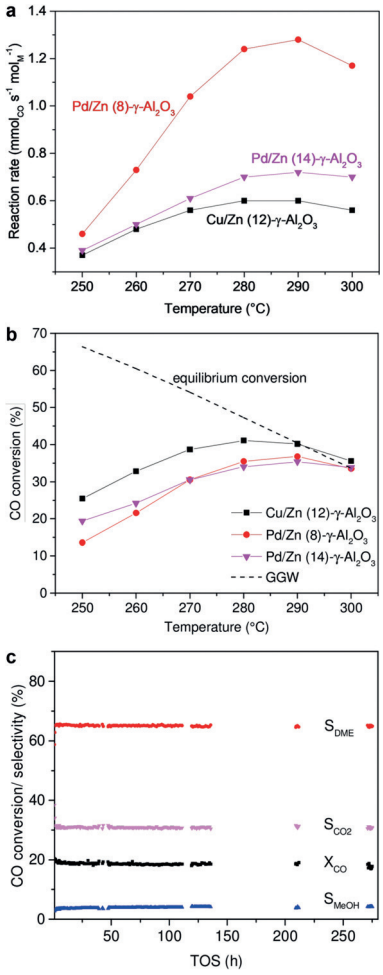

Figure 2. a) Reaction rates and b) CO conversions for STD catalysts derived from Pd/Zn and Cu/Zn NPs (50 bar, H_2:CO = 1, 70 vol% inert gases). c) Conversion and selectivity with TOS (250 °C) (Pd/Zn (8)-γ-Al_2O_3).

performance.[11] Interestingly, the reaction rate normalized to amount of Pd (in mol) was superior for Pd/Zn (8)-γ-Al_2O_3 compared to Pd/Zn (14)-γ-Al_2O_3 illustrating the influence of well-balanced catalyst functionalities. Pd/Zn (14)-γ-Al_2O_3 revealed S_{MeOH} of 9% (250 °C) indicating incomplete methanol dehydration, which is probably due to the lower γ-Al_2O_3 content (S_{MeOH} 3% for Pd/Zn (8)-γ-Al_2O_3; Supporting Information, Tables S1, S2; Figure S2). Therefore, less methanol was withdrawn from the equilibrium, and lower reaction rates compared to Pd/Zn (8)-γ-Al_2O_3 were observed. Compared to the Cu/Zn-based reference catalyst prepared via a similar synthetic approach, Pd/Zn catalysts showed enhanced CO turnover rates and less CH_4 formation (Figure 2a; Supporting Information, Figure S2).[10a] Most notably, the Pd-based catalysts showed excellent stability over time on stream (TOS; Figure 2c), with CO conversion and DME selectivity remaining constant after 270 h. After testing the catalyst at temperatures up to 300 °C, X_{CO} was reproducible at 250 °C. In contrast, the Cu/Zn-based reference catalyst revealed progressive deactivation (Supporting Information, Figure S3).[10a] Compared to Cu, both higher thermal stability of the intermetallic PdZn compound and higher hydrogenation activity of Pd may prevent particles sintering and deposition of carbonaceous species under these conditions, respectively.

Formation of the active catalyst phase under reducing H_2 atmosphere was monitored by in situ XAS at pressures up to 20 bar. XAS spectra (Figure 3a,b) recorded at room temperature approximately 3 min after switching to reducing H_2 flow showed complete reduction of PdO in the calcined catalyst (Figure 3c), while ZnO remained oxidized (Figure 3b,d; reference spectra, Supporting Information, Figure S3). The reduction of PdO_x NPs with H_2 at low temperatures has been

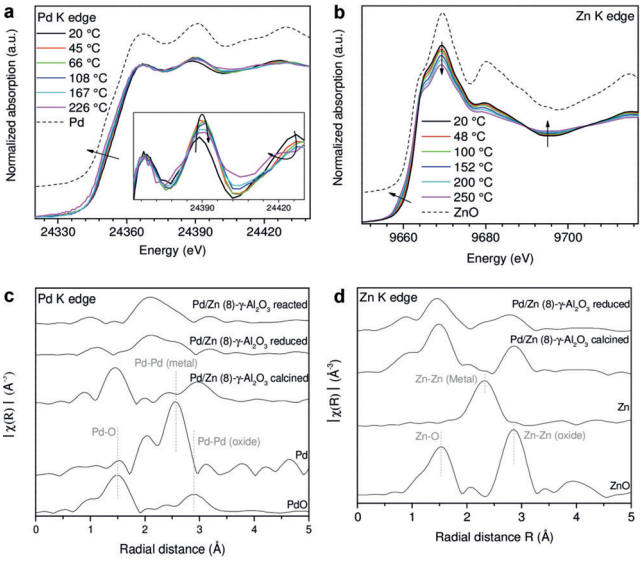

Figure 3. a),b) XANES spectra measured during in situ TPR experiments at a) Pd K and b) Zn K edges (RT to 250 °C; 5% H_2/He; heating rate 1 °C min^{-1}; Pd/Zn (8)-γ-Al_2O_3). c),d) FT k^2-weighted EXAFS spectra (not corrected for the phase shift) measured during in situ XAS experiments at c) Pd K and d) Zn K edges after calcination, reduction at 250 °C.

previously reported for Pd-based catalysts.[12] The X-ray absorption near edge structure (XANES) spectrum (20 °C, 5% H_2/He) showed a circa 0.8 eV shift of the rising edge to higher energies and shifts of all maxima to lower energies compared to the Pd^0 reference spectrum (Figure 3a). Since no reduction of Zn occurred at 20 °C, the observed shifts of the XANES features of Pd NPs could be attributed only to formation of PdH_x hydrides.[13] While extended X-ray absorption fine structure (EXAFS) is not sensitive to light atoms like hydrogen, Pd K edge XANES may be used to detect changes in the structure of unoccupied electronic states and is thus affected by the formation of PdH_x owing to mixing of unoccupied states of hydrogen and palladium.[14a] The observed shifts of the XANES features and the difference spectrum compared to metallic Pd (Supporting Information, Figure S4c) are consistent with the formation of PdH_x NPs.[14] They disappeared at 45 °C confirming decomposition of PdH_x to Pd^0 species (inset in Figure 3a; Supporting Information, Figure S4d). The Pd K edge position continuously shifted to lower energies during heating, probably caused by alloying of Pd with Zn via spillover of hydrogen from PdH_x NPs to the neighboring ZnO species.[13] No significant changes in the Pd K spectra occurred above 180 °C (Supporting Information, Figure S5a). Linear combination analysis (LCA, Supporting Information, Figure S5b) of the Zn K edge XANES spectra showed that a Pd^0:Zn^0 ratio of 1:1 was reached at 180 °C. The EXAFS region in the Pd K edge spectra exhibited pronounced changes until 250 °C, indicating alloying with Zn (Figure 3a). Gradual reduction of Zn was also observed during activation up to 250 °C (Figure 3b), where 31% (± 10%)[15] of ZnO was reduced to Zn^0. Following activation, the atomic Zn^0 to Pd^0 ratio was 1.3:1, suggesting the formation of alloyed PdZn NPs with an excess of Zn^0 species, probably on the surface of PdZn, favored by lower surface energy of Zn. This is further supported by the Fourier-transformed (FT) EXAFS (Figure 3c,d). At the Pd K edge, EXAFS revealed bond distances of 2.58 ± 0.03 Å (Pd–Zn) and 2.76 ± 0.03 Å (Pd–Pd) for the activated STD catalyst, indicating the formation of the PdZn phase during H_2 activation (Supporting Information, Figure S6, Table S3).[8]

The STD process was then studied at high pressure using operando XAS and reaction products monitored by on-line mass spectrometry (Supporting Information, Figure S4f). Spectra at Pd K edge were measured after the formation of methanol and DME had stabilized. The coordination numbers (CN, Supporting Information, Table S3, Figure S6) decreased from 7.1 (Pd-Zn) and 3.6 (Pd-Pd) in the H_2-activated catalyst to 5.5 (Pd-Zn) and 2.6 (Pd-Pd) during DME synthesis. The Pd-Zn to Pd-Pd CN ratio remained 2:1, in good agreement with the intermetallic bulk structure (Figure 1). Hence, the intermetallic PdZn phase remained stable during the STD process. A similar decrease in CN was reported by Tao et al.[16] for a pure Pd catalyst under CO and attributed to the formation of small clusters on the catalyst surface. The CN decrease observed herein suggests similarly an increase in dispersion or an increase in surface area. DFT calculations were performed on (adsorbate-induced) Pd segregation to investigate the surface structure under reaction conditions. They strongly indicate that the stability of the PdZn

intermetallic compound prevents segregation of Pd, even in the presence of CO and OH (Supporting Information, Table S4; Figure S7).

DFT calculations furthermore confirmed prominent reaction paths for a high activity of PdZn alloys in CO hydrogenation to methanol, similar as for Cu. For this purpose, a PdZn $L1_0$ slab model with (111) termination was used to calculate adsorption energies and transition states of the CO hydrogenation reaction (Figure 4a,b). Calculations of PdZn-(111) (red line) are compared to earlier calculations of CO hydrogenation on Cu(111) (black line) and Cu(211) (blue line) surfaces.[17] Although these calculations were performed with a different functional (RPBE)[18] than that used here (BEEF-vdW),[19] we note that calculations comparing RPBE and BEEF-vdW for CO hydrogenation on Cu(211) revealed almost identical results.[20] As shown in Figure 4a, the strength with which intermediates and transition states are bound to the PdZn surface are strikingly similar to those calculated for Cu(211), which is believed to be the active site in CO hydrogenation.[17,21] In an attempt to understand why PdZn surfaces have common properties to that observed for Cu, we investigated the d-projected density of states (DOS) and the corresponding d-band center often used as a descriptor of surface reactivity.[22] The d-projected DOS of PdZn is compared with the DOS of Cu(111) and Pd(111) in Figure 4c. The d-states of Pd(111) are not fully filled, resulting in a d-band center of −1.73 eV, similar to earlier reports.[23] For PdZn, however, the d-band is now completely filled and shifted downwards resulting in a d-band center of −2.32 eV. This is again strikingly similar to the −2.40 eV obtained for Cu(111) (note that the d-band of Cu(211) is even closer; −2.35 eV; Supporting Information, Figure S8). The local density of states of Pd in a PdZn alloy are thus similar to those of Cu, as also reported earlier.[24]

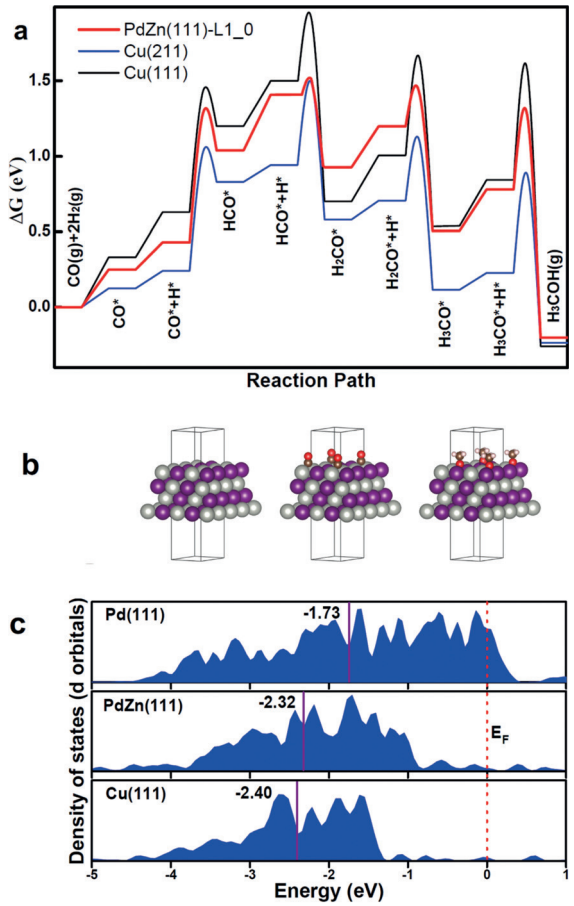

Figure 4. a) Gibbs-free energy diagram for CO hydrogenation on Cu-(111), Cu(211), and PdZn(111)-$L1_0$. Gibbs free energies are calculated for $T = 500$ K, $p(H_2) = 40$ bar, $p(CO) = 10$ bar, and $p(CH_3OH) = 1$ bar. Values for the Cu(111) and Cu(211) are taken from Ref. [16]. b) PdZn-(111)-$L1_0$ surface model (Pd light gray, Zn purple, O red, C brown), c) DOS calculated for Cu(111), Pd(111), and PdZn(111)-$L1_0$. Calculated d band centers are marked with dark red line.

In conclusion, uniform Pd/Zn-based NPs with a reactive Pd^0–Zn^{2+} interface ensured the formation of intermetallic PdZn NPs during in situ activation and provided the key building blocks for the methanol active component in bifunctional STD catalysts. High-pressure operando XAS studies suggest intermetallic PdZn NPs as the methanol active species and DFT calculations confirm that these alloys are indeed highly active in CO hydrogenation to methanol. Enhanced stability and longevity can be achieved even at higher reaction temperature (300 °C) with STD catalysts based on such intermetallic PdZn particles, while ensuring both high product and low methane selectivities.

Acknowledgements

M.G. acknowledges financial support of the Helmholtz Research School "Energy-Related Catalysis". H.L., J.J., and F.S. gratefully acknowledge support by the state of Baden-Württemberg through bwHPC (bwunicluster and JUSTUS, RV bw16G001 and bwl17D011). H.L. acknowledges funding by the National Natural Science Foundation of China. We thank the CAT-ACT beamline at the synchrotron radiation source at KIT for beamtime and Dr. T. Prüßmann for support during measurements. The STN and SCI programs are acknowledged for financial support of the high pressure XAFS infrastructure. We thank D. Neumann-Walter and Dr. T. Otto for support with BET measurements and Dr. Ch. Kübel, Institute of Nanotechnology, and the Karlsruhe Nano Micro Facility (KNMF, KIT) for HRTEM.

Conflict of interest

The authors declare no conflict of interest.

Keywords: bifunctional catalysts · density functional calculations · dimethyl ether synthesis · operando XAS · Pd/Zn nanoparticles

How to cite: *Angew. Chem. Int. Ed.* **2019**, *58*, 15655–15659
Angew. Chem. **2019**, *131*, 15802–15806

[1] a) J. Sun, G. Yang, Y. Yoneyama, N. Tsubaki, *ACS Catal.* **2014**, *4*, 3346–3356; b) http://www.methanol.org/wp-content/uploads/

2016/06/DME-An-Emerging-Global-Guel-FS.pdf, May 20, 2109).
[2] M. Stiefel, R. Ahmad, U. Arnold, M. Döring, *Fuel Process. Technol.* **2011**, *92*, 1466 – 1474.
[3] a) Q. Ge, Y. Huang, F. Qiu, S. Li, *Appl. Catal. A* **1998**, *167*, 23 – 30; b) V. M. Lebarbier, R. A. Dagle, L. Kovarik, J. A. Lizarazo-Adarme, D. L. King, D. R. Palo, *Catal. Sci. Technol.* **2012**, *2*, 2116 – 2127.
[4] a) A. T. Aguayo, J. Ereña, I. Sierra, M. Olazar, J. Bilbao, *Catal. Today* **2005**, *106*, 265 – 270; b) H. H. Kung, *Catal. Today* **1992**, *11*, 443 – 453; c) T. Lunkenbein, F. Girgsdies, T. Kandemir, N. Thomas, M. Behrens, R. Schlögl, E. Frei, *Angew. Chem. Int. Ed.* **2016**, *55*, 12708 – 12712; *Angew. Chem.* **2016**, *128*, 12900 – 12904; d) O. Martin, C. Mondelli, D. Curulla-Ferré, C. Drouilly, R. Hauert, J. Pérez-Ramírez, *ACS Catal.* **2015**, *5*, 5607 – 5616.
[5] R. A. Dagle, Y.-H. Chin, Y. Wang, *Top. Catal.* **2007**, *46*, 358 – 362.
[6] L. Bollmann, J. L. Ratts, A. M. Joshi, W. D. Williams, J. Pazmino, Y. V. Joshi, J. T. Miller, A. J. Kropf, W. N. Delgass, F. H. Ribeiro, *J. Catal.* **2008**, *257*, 43 – 54.
[7] H. Bahruji, M. Bowker, W. Jones, J. Hayward, J. Ruiz Esquius, D. J. Morgan, G. J. Hutchings, *Faraday Discuss.* **2017**, *197*, 309 – 324.
[8] M. W. Tew, H. Emerich, J. A. van Bokhoven, *J. Phys. Chem. C* **2011**, *115*, 8457 – 8465.
[9] A. Ota, E. L. Kunkes, I. Kasatkin, E. Groppo, D. Ferri, B. Poceiro, R. M. Navarro Yerga, M. Behrens, *J. Catal.* **2012**, *293*, 27 – 38.
[10] a) M. Gentzen, W. Habicht, D. E. Doronkin, J. D. Grunwaldt, J. Sauer, S. Behrens, *Catal. Sci. Technol.* **2016**, *6*, 1054 – 1063; b) M. Gentzen, D. E. Doronkin, T. L. Sheppard, J. D. Grunwaldt, J. Sauer, S. Behrens, *Appl. Catal. A* **2018**, *557*, 99 – 107; c) M. Gentzen, D. E. Doronkin, T. L. Sheppard, J.-D. Grunwaldt, J. Sauer, S. Behrens, *Appl. Catal. A* **2018**, *562*, 206 – 214; d) S. Schimpf, A. Rittermeier, X. N. Zhang, Z. A. Li, M. Spasova, M. van den Berg, M. Farle, Y. Wang, R. A. Fischer, M. Muhler, *ChemCatChem* **2010**, *2*, 214 – 222.
[11] J.-H. Fei, X.-J. Tang, Z.-Y. Huo, H. Lou, X.-M. Zheng, *Catal. Commun.* **2006**, *7*, 827 – 831.
[12] J.-D. Grunwaldt, B. Kimmerle, S. Hannemann, A. Baiker, P. Boye, C. G. Schroer, *J. Mater. Chem.* **2007**, *17*, 2603 – 2606.
[13] M. Armbrüster, M. Behrens, K. Föttinger, M. Friedrich, É. Gaudry, S. Matam, H. Sharma, *Catal. Rev.* **2013**, *55*, 289 – 367.
[14] a) A. L. Bugaev, A. A. Guda, A. Lazzarini, K. A. Lomachenko, E. Groppo, R. Pellegrini, A. Piovano, H. Emerich, A. V. Soldatov, L. A. Bugaev, V. P. Dmitriev, J. A. van Bokhoven, C. Lamberti, *Catal. Today* **2017**, *283*, 119 – 126; b) A. L. Bugaev, O. A. Usoltsev, A. Lazzarini, K. A. Lomachenko, A. A. Guda, R. Pellegrini, M. Carosso, J. G. Vitillo, E. Groppo, J. A. van Bokhoven, A. V. Soldatov, C. Lamberti, *Faraday Discuss.* **2018**, *208*, 187 – 205; c) M. Selinsek, B. J. Deschner, D. E. Doronkin, T. L. Sheppard, J.-D. Grunwaldt, R. Dittmeyer, *ACS Catal.* **2018**, *8*, 2546 – 2557.
[15] J. Timoshenko, A. Shivhare, R. W. J. Scott, D. Lu, A. I. Frenkel, *Phys. Chem. Chem. Phys.* **2016**, *18*, 19621 – 19630.
[16] F. F. Tao, L. Nguyen, S. Zhang, Y. Li, Y. Tang, L. Zhang, A. I. Frenkel, Y. Xia, M. Salmeron, *Nano Lett.* **2016**, *16*, 5001 – 5009.
[17] M. Behrens, F. Studt, I. Kasatkin, S. Kühl, M. Hävecker, F. Abild-Pedersen, S. Zander, F. Girgsdies, P. Kurr, B.-L. Kniep, M. Tovar, R. W. Fischer, J. K. Nørskov, R. Schlögl, *Science* **2012**, *336*, 893 – 897.
[18] B. Hammer, L. B. Hansen, J. K. Nørskov, *Phys. Rev. B* **1999**, *59*, 7413 – 7421.
[19] J. Wellendorff, K. T. Lundgaard, A. Møgelhøj, V. Petzold, D. D. Landis, J. K. Nørskov, T. Bligaard, K. W. Jacobsen, *Phys. Rev. B* **2012**, *85*, 235149.
[20] F. Studt, F. Abild-Pedersen, J. B. Varley, J. K. Nørskov, *Catal. Lett.* **2013**, *143*, 71 – 73.
[21] F. Studt, M. Behrens, E. L. Kunkes, N. Thomas, S. Zander, A. Tarasov, J. Schumann, E. Frei, J. B. Varley, F. Abild-Pedersen, J. K. Nørskov, R. Schlögl, *ChemCatChem* **2015**, *7*, 1105 – 1111.
[22] a) B. Hammer, J. K. Norskov, *Nature* **1995**, *376*, 238; b) B. Hammer, J. K. Nørskov, *Surf. Sci.* **1995**, *343*, 211 – 220.
[23] H. Xin, A. Vojvodic, J. Voss, J. K. Nørskov, F. Abild-Pedersen, *Phys. Rev. B* **2014**, *89*, 115114.
[24] Z.-X. Chen, K. M. Neyman, A. B. Gordienko, N. Rösch, *Phys. Rev. B* **2003**, *68*, 075417.

Manuscript received: May 20, 2019
Revised manuscript received: July 23, 2019
Accepted manuscript online: August 8, 2019
Version of record online: September 19, 2019

